

Silicon-nitride nanosensors toward room temperature quantum optomechanics

Enrico Serra,^{1,2,3,a)} Antonio Borrielli,^{2,1} Francesco Marin,^{4,5,6,7} Francesco Marino,^{5,6} Nicola Malossi,^{8,9} Bruno Morana,³ Paolo Piergentili,^{8,9} Giovanni Andrea Prodi,¹⁰ Lina Sarro,³ Paolo Vezio,^{5,6} David Vitali,^{8,9} and Michele Bonaldi^{1,2}

¹⁾*Istituto Nazionale di Fisica Nucleare (INFN), Trento Institute for Fundamental Physics and Application, 38123 Povo, Trento, Italy*

²⁾*Institute of Materials for Electronics and Magnetism, Nanoscience-Trento-FBK Division, 38123 Povo, Trento, Italy*

³⁾*Department of Microelectronics, Delft University of Technology, Feldmannweg 17, 2628 CT Delft, The Netherlands*

⁴⁾*European Laboratory for Non-Linear Spectroscopy (LENS), Via Carrara 1, I-50019 Sesto Fiorentino (FI), Italy*

⁵⁾*CNR-INO, L.go Enrico Fermi 6, I-50125 Firenze, Italy*

⁶⁾*INFN, Sezione di Firenze*

⁷⁾*Dipartimento di Fisica e Astronomia, Università di Firenze, Via Sansone 1, I-50019 Sesto Fiorentino (FI), Italy*

⁸⁾*Physics Division, School of Science and Technology, University of Camerino, I-62032 Camerino (MC), Italy*

⁹⁾*INFN, Sezione di Perugia, via A. Pascoli, I-06123 Perugia, Italy*

¹⁰⁾*Dipartimento di Fisica, Università di Trento, I-38123 Povo, Trento, Italy*

(Dated: 30 April 2021)

Observation of quantum phenomena in cryogenic, optically cooled mechanical resonators has been recently achieved by a few experiments based on cavity optomechanics. A well-established experimental platform is based on a thin film stoichiometric (Si_3N_4) nanomembrane embedded in a Fabry-Perot cavity, where the coupling with the light field is provided by the radiation pressure of the light impinging on the membrane surface. Two crucial parameters have to be optimized to ensure that these systems work at the quantum level: the cooperativity C describing the optomechanical coupling and the product $Q \times \nu$ (quality factor - resonance frequency) related to the decoherence rate. A significant increase of the latter can be obtained with high aspect-ratio membrane resonators where uniform stress dilutes the mechanical dissipation. Furthermore, ultra-high $Q \times \nu$ can be reached by drastically reducing the edge dissipation via clamp-tapering and/or by soft-clamping, virtually a clamp-free resonator configuration. In this work, we investigate, theoretically and experimentally, the edge loss mechanisms comparing two state-of-the-art resonators built by standard micro/nanofabrication techniques. The corresponding results would provide meaningful guidelines for designing new ultra-coherent resonating devices.

I. INTRODUCTION

A significant boost in the performance of sensors and metrological protocols can come from the use of quantum optomechanical sensors. In fact, quantum-enhanced metrology allows measurements with a precision that surpasses any classical limitation, enabling a generation of sensors of unprecedented sensitivity. Optomechanical resonators made possible the measurement of continuous force and displacement below the standard quantum limit with SiN membranes,¹ sensing forces at the attonewton level with phononic crystal silicon nitride nanobeams,² the quantum non demolition measurement of optical field fluctuations with a highly reflective silicon resonator.³ The domain of application of quantum-enhanced devices ranges from fundamental physics experiments, as the search for quantum gravity effects or the detection of weak stochastic forces,^{4,5} to quantum technology applications. In fact, adding an electrical degree of freedom (like an electrode)

to the mechanical device, one can realize bidirectional frequency electro-opto-mechanical modulators to convert optical signals, or ultrasensitive transducers for a shot-noise limited nuclear magnetic resonance (NMR).⁶ These kind of hybrid-devices are gaining momentum in foreseen quantum networks due to their peculiar property of maintaining the quantum coherence for very long times.⁷

A wide variety of mechanical oscillators can be designed and coupled with a light field, like silicon optomechanical crystals, silica microtoroids, silicon nitride nanobeams or nanomembranes, with masses ranging from μg to pg and frequencies from kHz to GHz.⁸ In general, quantum properties of all optomechanical system are hidden and/or destroyed by thermal noise. For this reason, all quantum effects observed to date have been obtained on resonators placed in a cryogenic environment. Unfortunately this requirement is a major obstacle to the realization of exploitable sensors, therefore a recent branch of research and few recent experiments on levitated nanospheres,⁹⁻¹² are progressing toward a new generation of optomechanical systems, able to maintain a quantum behavior even at room temperature. Actually, to facilitate room temperature optomechanics, two major parameters

^{a)}Electronic mail: E.Serra@tudelft.nl

should be improved: the optomechanical cooperativity C , proportional to the optomechanical interaction strength, and the $Q \times \nu$ product, inversely proportional to the coupling between the resonator and the surrounding thermal bath. When the cooperativity C is larger than the number of quanta in the mechanical resonator $n_{th} \cong k_B T / \hbar \nu$, the phonon-photon transfer is faster than the decoherence rate due phonon leakage from the resonator to the thermal bath. Cooperativity is defined as the ratio between the square of the coherent coupling rate g and the product between the optical (κ) and mechanical (γ) dissipation rates: $C = 4g^2 / \kappa\gamma$ where $g = g_0 \sqrt{n_c}$, with n_c the intracavity photon number, g_0 the single-photon coupling rate. Hence, improving cooperativity means reducing losses and improving the optomechanical interaction. In turn, reducing losses improves the number of coherent oscillations the resonator can undergo before one environmental phonon enters the system, which is just the product $Q \times \nu$. If we compare this figure with the thermal decoherence rate $k_B T / (Q\hbar)$, we easily find the condition for neglecting thermal decoherence over one mechanical period, that is $Q \times \nu > 6.2$ THz at room temperature.

Usually the resonators is embedded into a high-finesse optical Fabry-Perot cavity, where interaction between photons and phonons takes place. The cavity is externally pumped with a monochromatic laser source (for example a Nd:YAG IR laser) and the radiation pressure exerted by the optical field on the vibrating device generates intensity cavity field fluctuations containing information about its displacement. This technique has been used to probe a wide variety of physical phenomena.⁸ In the classical domain we have studied parametric squeezing of mechanical motion induced by optical field modulation,¹³ while in the quantum domain we have harnessed the optomechanical interaction to make a quantum non-demolition measurements of optical fields,³ and more recently we explored the border between classical and quantum physics by observing the quantum signature of a squeezed mechanical oscillator.¹⁴

In this work we focus on resonators based on stoichiometric Si_3N_4 membranes, commonly used in optomechanical setups. Here to comply with the requirement $Q \times \nu > 6.2$ THz, needed for room temperature cavity optomechanics, the membrane is tensioned to dilute the mechanical dissipation, in a scheme first proposed in the mirror suspensions of gravitational wave antennae.¹⁵ Thanks to this effect, nanobeams or nanomembranes made of thin nitride amorphous films, with intrinsic Q-factor of 4000, can reach ultra-high Q-factors of the order of 10^8 to 10^9 , if produced with an internal stress of about 1 GPa.^{16,17} However the dilution of the dissipation is a design strategy that can be exploited also in other materials and can be complemented by other strain engineering approaches. For instance, in III-V semiconductors ($GaAs$, $GaNAs$, and $In_{1-x}Ga_xP$), strain tunability is obtained by lattice mismatch between the films epitaxially grown and the substrate and also in this case the resulting tensile stress can exceed 1 GPa.¹⁸

In the following we compare the performances of two state-of-the-art designs for membrane resonators, considering the stress engineering framework, the fabrication issues and their ultimate performances in view of room temperature optome-

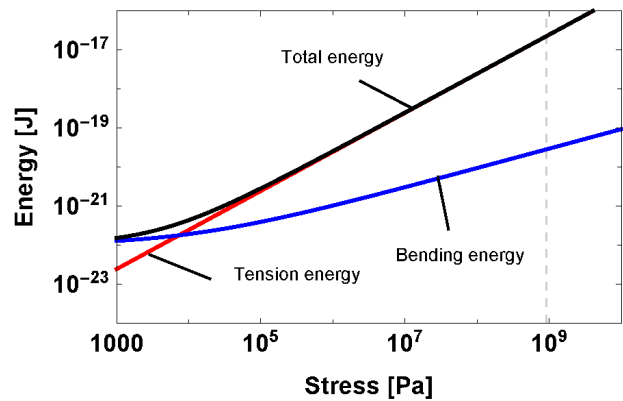


FIG. 1. Energy diagram for the (0,1) mode of a circular-shaped nanomembrane resonator with dimensions $D = 1480 \mu\text{m}$, thickness $h = 100 \text{ nm}$ showing the contribution of the tensile, the bending energy, and the total energies by varying the internal stress σ_0 .

chanics applications. We set out design rules that we plan to use in developing future ultra-high coherence devices.

II. DAMPING ANALYSIS

The total mechanical dissipation can be obtained as the incoherent sum of extrinsic (for instance gas damping and clamping losses), and internal contributions. Internal losses can be classified into the following categories: intrinsic dissipation originated from the delay between strain and stress in the material, thermoelastic loss with local heat generation and conduction, and Akhiezer damping due to coupling between the strain field and the phonon modes. In devices based on Si_3N_4 membranes the intrinsic dissipation determines the ultimate sensitivity of the device, as thermoelastic and Akhiezer losses are at least one order of magnitude lower than the intrinsic losses in case of silicon nitride.¹⁹ Clamping losses are also negligible in the considered devices, thanks to the use of on-chip seismic filtering stage or phononic bandgap crystal effectively isolating the membrane from its frame.^{20,21}

A. Dissipation dilution by uniform stress

A static strain ϵ_0 originates in a Si_3N_4 film from the mismatch between the linear expansion coefficient of the nitride layer and the substrate during the cooling phase that follows the Low Pressure Chemical Vapor Deposition (LPCVD) process. As a consequence, a biaxial state of stress σ_0 builds up in the film and reduces the intrinsic mechanical dissipation. After the first observations by Southworth,²² this effect has been theoretically investigated for 1D or 2D micro- and nano-mechanical resonators (strings or membranes) showing that the stress "dilutes" intrinsic dissipation, thanks to the increase of the oscillator resonant frequency while bending losses remain essentially constant.^{17,23} A more recent approach made clear that the Q-factor increase can be evaluated as the ratio

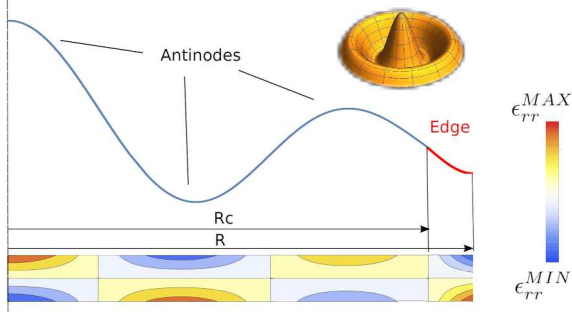


FIG. 2. Cross-section of a circular membrane showing the radial bending strain (ϵ_{rr}) contour plot along thickness in case of an axisymmetric mode (0,3). Antinodes strain (distributed loss) in the region $(0, R_c)$ and edge strain (edge loss) in the region (R_c, R) (not in scale) are shown.

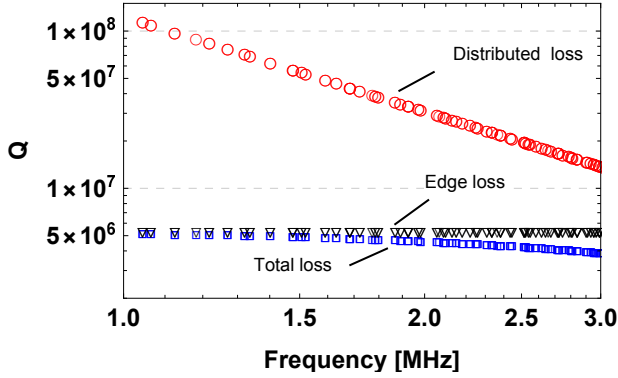


FIG. 3. Expected Q-factor for a circular-shaped membranes (dimensions $D = 1480 \mu\text{m}$, thickness $h = 100 \text{ nm}$, $\sigma_0 = 0.915 \text{ GPa}$) when edge (black-triangles), distributed (red-circles) or total loss (blue-squares) contributions are considered.

between the total elastic energy due to internal stress σ_0 and the bending energy:²⁵

$$\frac{Q}{Q_{int}} = \frac{W_{tens}}{W_{bend-edge} + W_{bend-internal}} \quad (1)$$

where Q_{int} is the intrinsic Q-factor (when $\sigma_0 = 0$) and in the bending energy, we have separated the contribution from the edge to that of the internal region of the resonator. Fig. 1 shows the energy balance for the fundamental mode of a 2-D membrane with dimension $D = 1480 \mu\text{m}$ and thickness $h = 100 \text{ nm}$ as a function of the tensile stress. As it is possible to fabricate films with a stress level in excess of 1 GPa, it is easy to produce a device dominated by tensile energy.

B. Edge and distributed dissipation

As pointed out by Schmid and Yu,^{17,23} intrinsic dissipation can be separated in the sum of two fundamental contributions: one due to the bending at the clamping edge of the membrane and the other one coming from the internal area,

mainly at the antinodes where local bending is higher as reported in Fig. 2 for a circular membrane. Edge dissipation is frequency independent while the internal contribution increases with modal index as it is shown in Fig. 3. Analytical approaches for evaluating the total intrinsic loss were first developed for 1-D doubly clamped beams and then extended to 2-D nanomembranes,²³ while in a general approach for numerically estimating intrinsic dissipation of 3-D structures is discussed.²⁵ In the anelastic loss model the stress σ is delayed with respect to the strain ϵ : $\sigma = (Y + i\phi Y)\epsilon$, where the loss angle is related to the Q-factor as $\phi = Q^{-1}$, therefore the dissipation is determined by the mean curvature. To clarify the role of edge dissipation in the total loss budget, we focus on the curvature in case of 1-D tensioned doubly-clamped nanostrip of length L , thickness k and width w :

$$YI_z \frac{d^4 u_n}{dx^4} - \sigma_0 L w \frac{d^2 u_n}{dx^2} - \rho \omega_n^2 u_n = 0 \quad (2)$$

where $YI_z = \frac{Yh^3 w}{12}$ is the flexural rigidity, u_n is the modal shape function and σ_0 the internal stress. At the clamping point the inertial term $\rho \omega_n^2 u_n$ is negligible, and the mean curvature at the edge can be approximated as:

$$\frac{d^2 u_{cl,n}(x)}{dx^2} = \left(\frac{du_n}{dx} \right)_{x=+0} \frac{1}{\lambda L} \exp\left(-\frac{x}{\lambda L}\right) \quad (3)$$

where $\lambda = \sqrt{1/12\epsilon_0} h/L$ is known as dilution factor, essentially the ratio between bending and elongation energies. From Eq. (3) the shape function at the clamping edge experiences a sharp exponential bending. The derivative $du_n/dx(0+)$ cannot be zero, because far from the clamping points the bending term can be neglected and the solution of Eq. (2) has a sinusoidal shape, that has to be connected with the solution at the clamping $u_{cl,n}$ containing the exponential term. In high-strain limit we have $\lambda \ll 1$ both in string and membranes and the critical region close to the clamping edges can be estimated as: $L_{cl} = \sqrt{Y/(12\sigma_0)} h \approx 5h = 500 \text{ nm}$ for $h=100 \text{ nm}$. Therefore, the edge loss involves only a small region where major dissipation takes place. The procedure described above can be extended to 3-D square membrane of side L by solving the general equation for vibrational plates written in terms of adimensional coordinates (η, χ) :

$$\lambda^2 \nabla_{\eta, \chi}^4 w_{nm} - \nabla_{\eta, \chi}^2 w_{nm} - \Omega^2 w_{nm} = 0 \quad (4)$$

where w_{nm} represents the displacement in the direction orthogonal to the membrane's plane, Ω the normalized frequency and $\lambda^2 = D/(\sigma_0 h L^2)$ is still the dilution parameter, now expressed in terms of the flexural rigidity of the plate D . From Eq. (4) the Q-factor has been derived for a square-shaped membrane as the sum of the edge and distributed contributions:²³

$$\frac{Q}{Q_{int}} = (2\lambda + (n^2 + m^2)\pi^2 \lambda^2)^{-1} \quad (5)$$

where Q_{int} is the intrinsic Q-factor (without dilution effect), n, m the modal indexes. In the following of the paper we analyze and discuss the interplay between these two dissipation mechanisms for the two devices presented in this work.

C. Circular membranes and modal expansion

In case of a circular membrane of radius R , the solutions of Eq. 4 are the Bessel functions J_m

$$w_{mn}(r, \theta) = k_{mn} J_m(\alpha_{mn} \frac{r}{R}) \cos(m\theta) \quad (6)$$

Where (r, θ) is the cylindrical coordinate system centered in the membrane with \mathbf{i}_z aligned along the membrane's out-of-plane axis. α_{mn} is the n -th root of the Bessel polynomial of order m . The constant k_{mn} is fixed by the normalization requirement:

$$h \int_S dS \rho w_{mn}^2(r, \theta) = M \quad (7)$$

as

$$k_{mn} = \sqrt{\frac{\pi R^2}{\int_S dS J_m^2(\alpha_{mn} \frac{r}{R}) \cos^2(m\theta)}} \quad (8)$$

where h is the membrane's thickness and M its mass. In the context of the modal expansion theory,²⁴ spatial variables can be separated from the temporal ones. Therefore the displacement of the membrane $u(r, \theta, t)$ can be written as a superposition of normal modes with time dependent coefficients

$$u(r, \theta, t) = \sum_{mn} a_{mn}(t) w_{mn}(r, \theta) \quad (9)$$

The membrane is then sampled on its surface by a readout with output X

$$X(t) = \int_S dS P_s(r, \theta) u(r, \theta, t) \quad (10)$$

where P_s is the weight function of the readout, normalized such that $\int_S dS P_s(r, \theta) = 1$ and depending on the measurement technology adopted. For instance, an optical readout based on laser beam is sensitive to the position of the membrane's surface, averaged over the gaussian beam profile with a waist w_0 :

$$P_s(r, \theta) = \frac{2}{\pi w_0^2} e^{-2r^2/w_0^2} \equiv \frac{2}{\pi w_0^2} e^{-2(x^2+y^2)/w_0^2} \quad (11)$$

The normalization choice Eq. (7) allows the convenient way of describing the motion of each mode w_{mn} as a harmonic oscillation with effective mass:

$$m_{mn}^{\text{eff}} = \frac{M}{(\int_S dS P_s(r, \theta) w_{mn}(r, \theta))^2} \quad (12)$$

From this equation it is easy to see that the lowest value of the effective mass is obtained when the readout samples a region of maximum oscillation amplitude (anti-node), while m_{mn}^{eff} increases if the readout samples a nodal region. For the $(0, n)$ axisymmetrical modes read by a laser beam centered on the membrane axis, the effective mass is:

$$m_{0n}^{\text{eff}} = \frac{M J_1^2(\alpha_{0n})}{2(\pi \int_0^R P(r) J_0(\alpha_{0n} \frac{r}{R}) r dr)^2} \quad (13)$$

where $M = \pi R^2 h \rho$ is the membrane physical mass, J_0, J_1 the two lowest order Bessel functions and α_{0n} the n -th root of J_0 . We remind that, in the pair of indexes (m, n) , the index m is the number of radial nodal lines and n is the number of circumferential nodal lines. In the lowest frequency drum mode $(0, 1)$, the circumferential node is the fixed edge. If the waist of the laser is much smaller than the membrane's radius, the first values of m_{0n}^{eff}/M are 0.269, 0.116, 0.074, 0.054. We note that the effective mass of the drum mode $(0, 1)$ is about 1/3 of the total membrane's mass.

D. Soft-clamped rectangular membranes

An effective method to reduce edge loss is to localize the vibrational modes away from the clamping region by soft-clamping. In this way we achieve a clamping-free device where edge losses can be neglected. Soft-clamping is a novel design strategy based on phononic crystals, proposed by Tsaturyan in case of a square-shaped membrane,²¹ and then applied to nanostrings.^{25,26} The bandgap of the phononic crystal is matched to the resonant frequency of the so called "defect modes" in the central part of the phononic structure (Fig. 3 and Fig. 4). A defect mode evanescently couple to the frame therefore eliminating the extra curvature at the edge imposed by the boundary conditions. Fig. 5 shows that the effectiveness of this soft-clamping depends on the number of phononic cells on the device: for instance with nine cells the displacement at the edge is reduced at least a factor of 100 w.r.t. the centre of the defect region. The Q-factor is limited only by the distributed losses when the edge contribution of the bending energy is neglected in Eq. (1). As a consequence, Q-factors in the bandgap region reach values in excess of 10^8 . Outside the bandgap the Q-factor of modes drop and is still limited by edge losses.

For a 1D string resonator of thickness h , Eq. (1) for the mode u_n is:

$$\begin{aligned} Q &= Q_{\text{int}} \frac{W_{\text{tens}}}{W_{\text{bend-internal}}} \\ &= Q_{\text{int}} \frac{\int_0^L \sigma(x) A(x) (\frac{du_n(x)}{dx})^2 dx}{\int_0^L Y I_z(x) (\frac{d^2 u_n(x)}{dx^2})^2 dx} \\ &= \eta \beta \frac{\sigma_0 a^2}{Y h} \end{aligned} \quad (14)$$

where σ_0 is the average stress, $A(x) = h(x)w$ the cross-section area, a the lattice parameter, L the string length, η a prefactor related to the mode shape and β is the average surface loss parameter. We point out that in this equation the intrinsic dissipation contribution is mainly due to surface losses $Q_{\text{int}}^{-1} = \frac{1}{\beta h}$. In fact surface loss is one of the damping mechanisms in micro- and nano-mechanical nitride resonators and its contribution dominates when the thickness h is less than 100 nm.²⁷

For a nanomembrane the analogous of the Eq. (14) be-

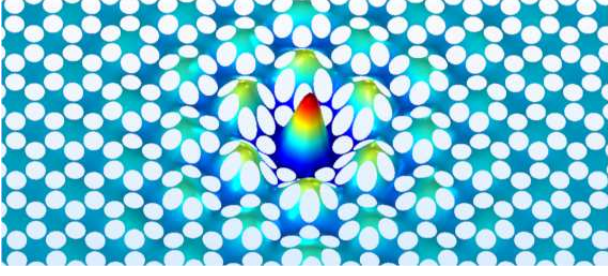


FIG. 4. Modal shape function of a bandgap mode A evaluated by a 3-D finite element simulation.

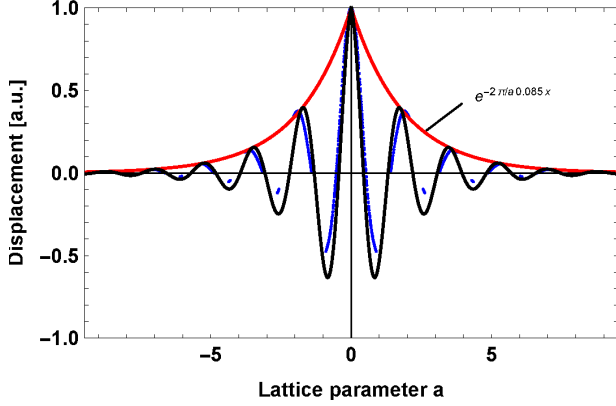


FIG. 5. The bandgap mode A cross-section along x axis. Blue curve is derived by FEM modal analysis, the red curve is an exponential function as a guide to the eye and the black is the sinusoidal decaying approximation, showing the evanescent decay.

comes:

$$\begin{aligned}
 Q &= Q_{int} \frac{W_{tens}}{W_{bend-internal}} = \\
 &= Q_{int} \frac{h \int_{-L_1/2}^{L_1/2} \int_{-L_2/2}^{L_2/2} \sigma(x,y) \left(\left(\frac{\partial w_{BG}(x,y)}{\partial x} \right)^2 + \left(\frac{\partial w_{BG}(x,y)}{\partial y} \right)^2 \right) dx dy}{D_z \int_{-L_1/2}^{L_1/2} \int_{-L_2/2}^{L_2/2} \left(\frac{\partial^2 w_{BG}(x,y)}{\partial x^2} + \frac{\partial^2 w_{BG}(x,y)}{\partial y^2} \right)^2 dx dy} \\
 &= f(a) \times \frac{\sigma_0}{Y h^2} \times \frac{1}{\phi + \frac{1}{\beta h}} \quad (15)
 \end{aligned}$$

where w_{BG} is the modal shape function of a defect mode, $f(a)$ is numerically evaluated from the mode shape as a function of the lattice constant a and of the membrane size. In this case bulk loss parameter ϕ and surface loss parameter β concur to determine the overall dissipation of the mode. For a membrane with dimensions $L_1 = 19a$, $L_2 = 19.5a$, the shape of the bandgap mode A is:

$$\begin{aligned}
 w_A(x,y) &= k_A e^{(-2\pi/a 0.085 (|x|+|y|))} \times \\
 &\times \cos(2\pi/a 0.57 |x|) \cos(2\pi/a 0.57 |y|) \quad (16)
 \end{aligned}$$

where k_A is determined by the normalization requirement Eq. 7. This shape function is compared in Fig. 4 with a FEM evaluation. The effective modal mass for mode A can be estimated by numerically evaluating the eigenfunction by finite

elements or from the modal shape $w_A(x,y)$ as:

$$m_A^{eff} = \frac{M}{\left(\int_{-L_1/2}^{L_1/2} \int_{-L_2/2}^{L_2/2} P(x,y) w_i(x,y) dx dy \right)^2} \quad (17)$$

III. CHIP-SCALE OPTOMECHANICAL Si_3N_4 OSCILLATORS

In the following we describe the fabrication of a round-shaped nanomembrane with an on-chip isolation stage^{20, 28} and a rectangular-shaped geometry endowed with a phononic bandgap structure²¹, both designed and produced in our microfabrication facility. The former is produced by bulk/surface micromachining using Deep-RIE and its quality factor is mainly limited by the edge losses, while the latter is produced by wet anisotropic KOH etching and is limited by distributed losses. Both membranes have an intrinsic stress of the order of 1 GPa, a dilution factor in the range $\lambda \simeq 10^{-4}$, and features a number of low loss mechanical modes resonating at frequencies in the MHz range with a modal effective mass in the range of pg to ng.

A. Round-shaped membrane with on-chip shield

Tensioned round-shaped membranes were produced with a uniform stress $\sigma_0 = 0.918 \pm 0.02$ GPa. The filtering structure shown in Fig. 6 was patterned on a 1 ± 0.025 mm thick Silicon-On-Insulator (SOI) wafer with Deep-RIE silicon etching Bosch process. We exploit the $2 \mu\text{m}$ thick buried oxide as etch stop layer when patterning the spring structure on the front side and the masses in the back side of the wafer. Additional metallic and dielectric sacrificial layers were used during processing to protect devices from scratching and from chemicals. All structures are patterned using contact aligner lithography and hard-contact exposure in the back side of the wafer. The membrane radius is defined by the re-entrant sidewall slopes of successive Deep-RIE steps that enlarges the central hole patterned using lithography. Depending on the details of the etching procedure, diameter in the range $1500 \pm 150 \mu\text{m}$ can be obtained. In order to evaluate possible effects of the edge dissipation on Q , we fabricated devices with two clamping conditions: membrane directly pinned to the silicon substrate (stitched membranes) and membrane without contact with the substrate. To this aim two oxides were used as sacrificial layers for the Deep-RIE last etching step: the LPCVD TEOS oxide shown in Fig. 6 (top) and the thermally grown oxide shown in Fig. 6 (bottom). In both cases the sacrificial oxide layer underneath the membrane was removed with an HF aqueous solutions and then rinsed with deionised water. Sticking is obtained by undercutting the LPCVD buried oxide below the edges of the window as demonstrated by Gopalakrishnan.²⁹ Fig. 7 shows, in case of non-stitched membrane, the initial undercut produced by HF etching of the oxide layer between the membrane and the substrate. The cross-section of the profile is irregular and wave-like but at a scale of hundreds of nanometers with respect to

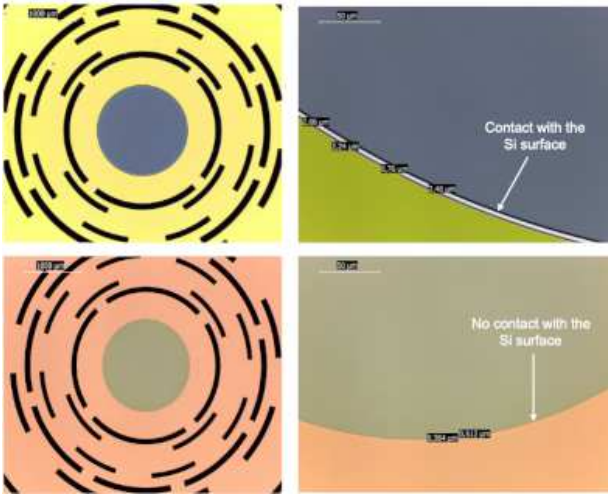


FIG. 6. Round-shaped Si_3N_4 membrane surrounded by the on-chip filter and detailed view of the membrane's edge. (Top) case of Si_3N_4 deposited on a LPCVD TEOS oxide sacrificial layer where the membrane is stitched on the Si substrate. (Bottom) case of Si_3N_4 deposited on a thermally grown oxide without membrane's stitching to the substrate.

mm scale of membrane's radius. Given the relatively large etching rate of LPCVD oxide, about three times greater than the thermally grown oxide, it is possible to obtain undercuts extending for $0.6 - 3 \mu\text{m}$ underneath the membrane. Membrane's stitching happens when the capillary forces of liquid trapped in the undercut region overcome the bending rigidity of the membrane. The undercut depth is observed to grow approximately linearly with etch time and we found that the minimum length to promote stitching is $0.6 \mu\text{m}$. Smoothness of the contact surfaces influences the edge losses as well as the presence of polymer residues from Deep-RIE process. To ensure repeatability over a number of devices and reduce edge loss, we made aggressive oxygen plasma steps after the last Deep-RIE step and flux DI water onto the membrane's edge after the HF release step.

B. Rectangular-shaped membrane with phononic bandgap

The device was fabricated following the process described by Tsaturyan,²¹ but we included two extra sacrificial layers to increase the process yield. The resulting membrane is 100 nm thick and is supported by a $14 \times 14 \text{ mm}^2$ silicon frame. Details of the structure are shown in Fig. 8. On the same wafer we made devices with different lattice constant $a = (160, 346, 360, 380) \mu\text{m}$, with corresponding overall membrane size $19a \times 19.5a$.

Devices were fabricated on a double-side polished $0.525 \pm 0.015 \text{ mm}$ thick wafer with roughness of 0.5 nm RMS . The tensioned LPCVD stoichiometric Si_3N_4 layer, with stress tuned to $0.918 \pm 0.02 \text{ GPa}$, was covered with $4 \mu\text{m}$ resist to pattern the phononic bandgap lattice by UV lithography in hard contact mode. The silicon nitride layer is then etched with fluorine based plasma. Note that the Si_3N_4 layer is

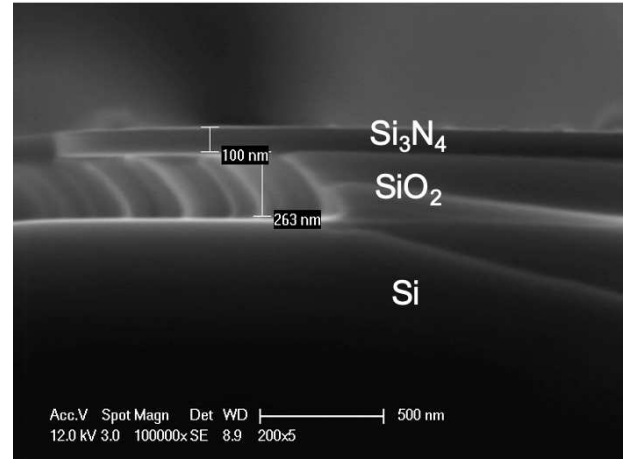


FIG. 7. SEM image at the edge of the membrane after partial breakage of a circular membrane showing the undercut of the oxide supporting the thin Si_3N_4 membrane.

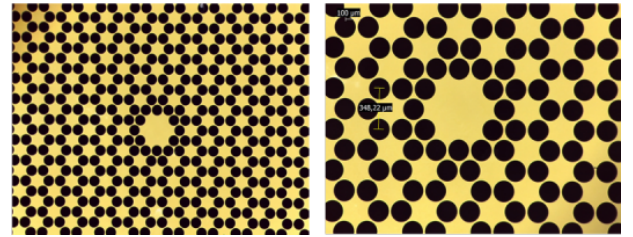


FIG. 8. Phononic bandgap lattice ($a=346 \mu\text{m}$) (left) with a detailed view of the central resonating part (right) with the hexagonal-shaped defect region in the centre of the lattice.

grown directly on the silicon surface without an oxide sacrificial layer as in case of round-shaped device. The bulk micromachining was done by KOH etching, and the sacrificial layers on the front side were removed by dry plasma and wet BHF etching. With hot DI water we remove residues from the KOH bath and clean the membrane surface. We point out that scratches or resist imperfections before UV lithography can trigger the membrane failure during the release phase, handling or dicing.

IV. Q-FACTOR MEASUREMENT WITH AN INTERFEROMETRIC SET-UP

The experimental set-up shown in Fig. 9 was designed to sense displacements at the thermal noise level for μg to mg-scale devices. It consists of a polarisation-sensitive Michelson interferometer followed by a balanced homodyne polarising detection. In details, following the scheme shown in Fig. 9, a polarising beam-splitter (PBS2) divides the beam into two parts, orthogonally polarised, forming the Michelson interferometer arms. The reference arm is focused to an electromagnetically-driven mirror M_1 , that is used for phase-locking the interferometer in the condition of maximum displacement sensitivity. The sensing arm is instead focused with

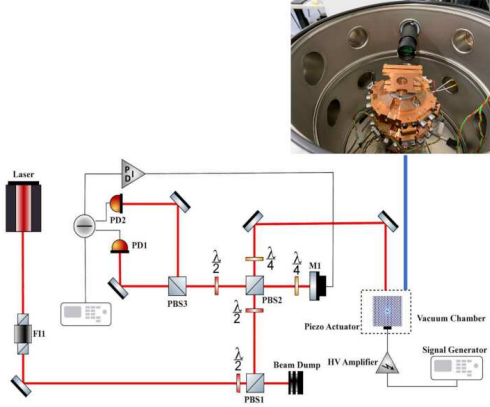


FIG. 9. High-sensitivity interferometer scheme for Q-factor measurements. (Top) Detailed view of the OFHC copper support for the resonators with the filtering suspension system clamped at the bottom of the vacuum chamber.

a waist below $100 \mu\text{m}$ on the oscillator kept in a vacuum chamber at a pressure of 10^{-6} mbar. After the reflection and a double pass through a quarter-wave plate, both beams suffer a 90° rotation of their polarisation, then they are completely transmitted (reference beam) or reflected (sensing beam) by the PBS2. The overlapped beams are then monitored by a homodyne detection, consisting of a half-wave plate, rotating the polarisations by 45° , and a polarising beam-splitter (PBS3) that divides the radiation into two equal parts sent to the photodiodes PD1 and PD2, whose outputs are subtracted. The signal obtained is a null-average, sinusoidal function of the path difference in the interferometer. Such a scheme is barely sensitive to laser power fluctuations. The difference signal is used as error signal in the locking servo-loop (the locking bandwidth is about 300 Hz) and also sent to the acquisition and measurement instruments. In order to measure the Q-factor we first drive the system at the resonance frequency ν_m by a piezoelectric actuator mounted on the sample holder, then remove the drive and acquire the amplitude of the displacement signal using the interferometer. The mechanical vibration follows an exponentially damped decay whose envelope amplitude varies according to: $u(t) = u_0 \exp(-t/t_m)$ where $t_m = Q/(\pi\nu_m)$ is the decay time of the mode.

V. MEMBRANE INSIDE AN OPTICAL CAVITY

The use of membrane oscillators in high sensitivity optomechanical nanosensors implies that they should be located inside high Finesse optical cavities, as partially reflecting surfaces. As a consequence, they should not spoil the cavity optical quality, and their overall mechanical noise (including the sensing mode and all the other mechanical modes) should be low enough to allow a stable frequency locking between the cavity optical resonance and the laser field. In order to test these requirements we have mounted the dices incorporating the membranes inside plano-concave cavities, using sil-

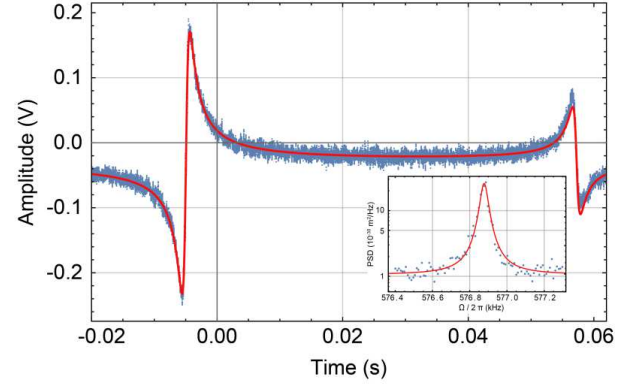


FIG. 10. Pound-Drever-Hall signal from an optical cavity containing a membrane with phononic bandgap structure. The distance between the carrier (right dispersive signal) and sideband (left signal) is 13.3 MHz, and is used to calibrate the frequency scan. Inset: power spectral density (PSD) of the A mode.

icon spacers between the membrane dice and the flat mirror to guarantee parallelism and mechanical stability. The round membranes with acoustic shield have been successfully used even inside helium flux cryostats, in quantum optomechanics experiments.^{10,31–33} Concerning the rectangular membranes with phononic bandgap structure, we have tested the PM-360 sample inside a 48 mm long cavity, in high vacuum at room temperature. We show in Fig. 10 the Pound-Drever-Hall signal obtained in this setup, by phase modulating the probe laser at 13.3 MHz. The fit to the data gives a cavity linewidth of 250 kHz (Finesse 12000), setting the bandgap modes in the resolved sidebands regime, with optical losses dominated by the input mirror transmission. The laser was then stably locked to the cavity. In the inset of the Fig. 10 we show a portion of the spectrum of the same Pound-Drever-Hall signal, exhibiting the resonance of the A mode, slightly optically cooled by an additional weak, red-detuned beam.

VI. RESULTS AND DISCUSSION

In this section we compare the performances of the two optomechanical sensors in terms of $Q \times v$ product and force sensitivity. We discuss advantages and drawbacks also in terms of modal density, surface's functionalization and microfabbrication process complexity.

A. Figure of merit $Q \times v$

In round-shaped membranes, modal frequencies are calculated by the well-known analytical formula: $\nu_{nm} = \frac{1}{\pi 2R} \alpha_{nm} \sqrt{\frac{\sigma}{\rho}}$ where α_{nm} is the root of the Bessel function J_m and (n, m) are the radial and circumferential modal indexes. For the rectangular membranes with phononic crystal, the modal frequencies are numerically evaluated by Finite Ele-

ment Analysis (FEA). The modal shapes of the five out-of-plane modes in the bandgap are shown in Fig. 11 where the first mode A is a singlet while (B, C) and (D, E) are doublets. Similarly to what shown for mode A in Fig. 4, all bandgap modes are well localized in the defect region and the displacement of the membrane fades out by going towards the edge, thus achieving the soft-clamping condition.

In Fig. 12 and 13 we compare the Power Spectral Density (PSD) of the displacement of the central area of the devices, measured for acoustic frequencies up to 2 MHz. Here the modes are driven by the thermal force to an amplitude depending upon the modal equivalent mass and upon the coupling with the laser beam.

In case of the round-shaped membrane, the normal modes are well separated and emerge from the background noise of 10^{-30} m²/Hz (Fig. 12). In general almost all expected modes can be found at the expected modal frequency; in the Figure we show for instance the position of the first drum mode (n,m)=(0,1). Here the filtering stage effectively decouples the frame from the membrane, as described by Borrielli,²⁰ hence the clamping losses are made negligible and the membrane dynamics is dominated by the intrinsic dissipation, both at the clamping edge and in the central area, for all mechanical modes. The Q factor is in the range between $5 - 10 \times 10^6$ and no differences could be appreciated in case of stitched and non-stitched membranes.

The rectangular-shaped membrane PSD spectrum, shown in Fig. 13, has a bandgap region with some distinct peaks emerging from the background noise (here at a level of 10^{-27} m²/Hz to 10^{-28} m²/Hz), each corresponding to the out-of-plane modes (A, B, C, D, E). In this case the Q-factor can be as high as 5×10^7 and scales down quadratically with the lattice constant a . In the region outside the bandgap the modal density dramatically increases due to a large number of resonances of the phononic crystal. For the bandgap modes we observed a dispersion of Q value in agreement with results obtained by Tsaturyan.²¹ In Table I we report the results for two rectangular-shaped membranes with lattice constant $a = 160$ μ m and of $a = 360$ μ m. The performances of the devices presented in this work are fully consistent with those presented by Tsaturyan,²¹ if the physical parameters of the membranes are properly scaled according to the theory presented in Sec. II D:

$$\nu = \hat{\nu} \times \frac{\hat{a}}{a} \sqrt{\frac{\sigma}{\hat{\sigma}}}, \quad Q = \hat{Q} \times \frac{\sigma \hat{h} a^2}{\hat{\sigma} \hat{h} \hat{a}^2} \quad (18)$$

where the parameters (ν, Q, h, a, σ) and $(\hat{\nu}, \hat{Q}, \hat{h}, \hat{a}, \hat{\sigma})$ identify two different geometrical configurations of the device. Some interesting considerations can be drawn by comparing the estimates obtained from the models developed in section II D with the measurements reported in Table I. In Fig. 14 we show the Q-factor measured for the mode A of a membrane with $\sigma = 0.918$ GPa, thickness $h = 100$ nm and lattice parameter $a = 360$ μ m, together with properly scaled values for similar devices.²¹ We also show the estimate obtained for mode A from the 2-D model Eqs (15) with $\phi = 2.66 \times 10^{-4}$ and $\beta = 60 \times 10^9$ m⁻¹. In Fig. 14 we compare the two devices in terms of the figure of merit $Q \times \nu$, that measures the co-

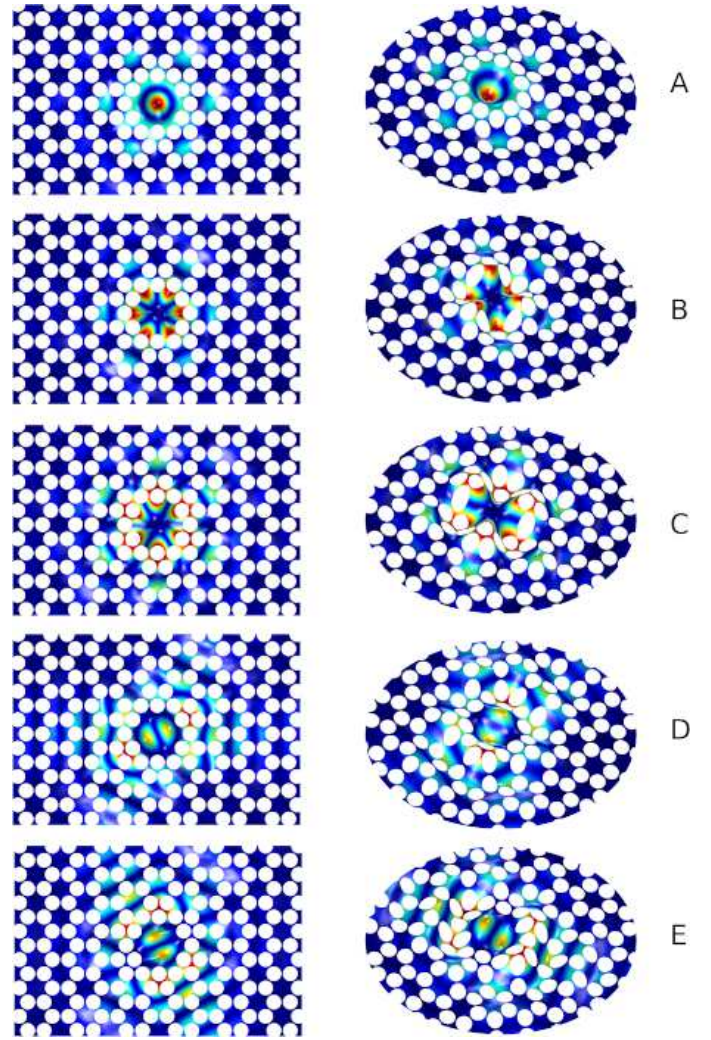


FIG. 11. FE modal analysis with $a = 160$ μ m of bandgap modes with frequencies $\nu_A > \nu_B > \nu_C > \nu_D > \nu_E$ showing that the defect mode evanescently couples to substrate at the edge (soft-clamping). Modes B and C and D and E are doublets.

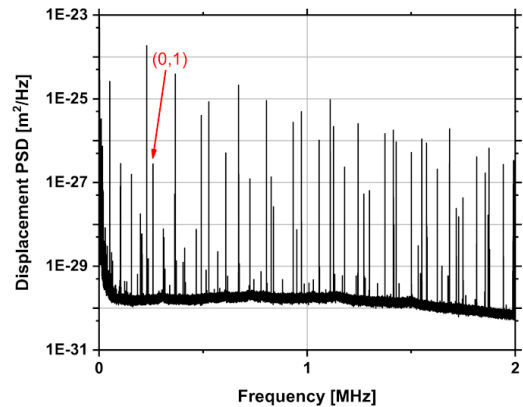


FIG. 12. Displacement PSD for the round-shaped membrane. Data are derived from the FFT of the interferometer output.

TABLE I. Measured Q-factor bandgap modes A, B, C, D, E for square-shaped membranes with lattice constant $a = 160,360 \mu\text{m}$ with membrane size $3040 \times 3120 \mu\text{m}^2$ and $6840 \times 7020 \mu\text{m}^2$ respectively.

MODE	PM-160			PM-360		
	ν [MHz]	Q 10^6	$\nu \times Q$ [THz]	ν [MHz]	Q 10^6	$\nu \times Q$ [THz]
A	1.23	11.2	11.19	0.571	19.3	11.02
B	1.32	10.4	13.73	0.614	11.0	6.75
C	1.34	11.5	15.41	0.620	54.0	33.48
D	1.41	3.2	4.48	0.649	10.3	6.68
E	1.43	11.4	16.30	–	–	–

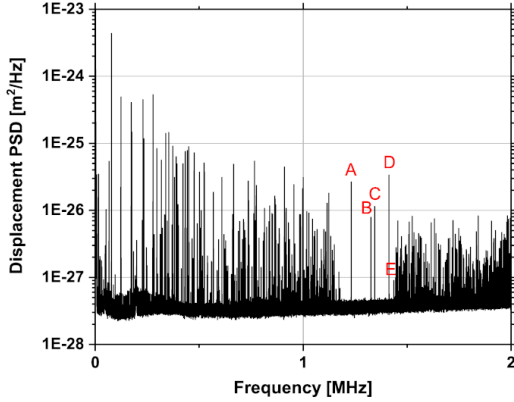


FIG. 13. Displacement PSD for a rectangular-shaped membrane with $a = 160 \mu\text{m}$. Data are derived from the FFT of the interferometer output.

herence rate. Devices with $Q \times \nu$ lying inside the gray area are compliant with the requirement for room temperature optomechanics, $Q \times \nu > 6.2 \text{ THz}$.⁸ Almost all modes of round-shaped membranes met the requirement, apart from some mode at low frequency. Bandgap modes of the rectangular-shaped membrane, where the quality factor is limited by the distributed loss mechanism, are fully compliant but more scattered results between the different modes, at least for what observed with the devices obtained with our production process. We point out that the quality factor can be tuned by changing the overall dimension of the device, as in larger membranes the edge loss becomes relatively smaller. On the other hand, we believe that this comparison is fair because we produced, for both kind of devices, the larger structures that could be hosted on our standard silicon frame $14 \times 14 \text{ mm}^2$.

B. Force sensitivity

The opto-mechanical membrane is an elastic body that vibrates due to the combined effects of the external forces, back-action radiation pressure and the thermal Langevin force. When the system is used as a probe for an external force, its sensitivity is limited by the equivalent input force density due to the technical noises. Given that we compare devices of different geometry and size, the evaluation must account for the precise shape of the surface sampled by the readout and for the point of application of the external force. Here we neglect readout backaction noise and consider only a force orthogonal to the membrane's plane and with a frequency equal to one of the membrane's resonances, say ω_n , but even the most general case could be evaluated, as done for instance in the context of resonant detectors of gravitational waves.³⁴

1. Generic force

Starting from the normal mode expansion (9), we evaluate the displacement of the membrane when a volume force density $\mathbf{G}(\mathbf{r})$ is applied to the membrane. The total driving force comes from the integration of this force density over the volume of the membrane V . If the time evolution of the force can be separated, we write:

$$\mathbf{G}(\mathbf{r}, t) = G_t(t) G_r(r, \theta, z) \mathbf{i}_z \quad (19)$$

where $G_t(t)$ is the total force applied to the membrane and G_r is a density function describing how the force field varies in the membrane's volume, with normalization:

$$\int_V dV G_r(r, \theta, z) = 1 \quad (20)$$

Thanks to the separability of time from spatial variables, the time evolution of the coefficient $a_n(t)$ is equivalent to the time development of a forced harmonic oscillator:

$$M \frac{\partial^2 a_n(t)}{\partial t^2} + M \omega_n^2 a_n(t) = G_t(t) \int_V dV G_r(r, \theta, z) w_n(r, \theta). \quad (21)$$

where $w_n(r, \theta)$ is constant along the membrane's thickness. Note that, in order not to burden the notation, we identify the mode by a single index n in this section. In the frequency domain (here and in the following we indicate the Fourier transform with a tilde) we have then:

$$\tilde{a}_n(\omega) = \frac{1}{M} \frac{\tilde{G}_t(\omega)}{(\omega_n^2 - \omega^2) + i\omega_n^2 \phi_n(\omega)} \int_V dV G_r(r, \theta, z) w_n(r, \theta) \quad (22)$$

where the system loss is modeled in the frequency domain by including explicitly the damping term $\phi_n = 1/Q_n$.¹⁵ If we consider the output coordinate X defined in Eq. (10), we see that, at the resonance ω_n , the response $T_G(\omega) = \tilde{X}/\tilde{G}_t$ of the oscillator to the external force density G is:

$$T_G(\omega_n) = -i \frac{Q_n}{M \omega_n^2} \int_V dV G_r(r, \theta, z) w_n(r, \theta) \times \int_S dS P_s(r, \theta) w_n(r, \theta) \quad (23)$$

where $P_s(r, \theta)$ is the weight function of the readout, defined in Eq. (11) for an optical readout.

2. Thermal noise and sensitivity

The fluctuation-dissipation theorem states that the one-side noise PSD of the coordinate X at the angular frequency ω is:

$$S_{XX}(\omega) = -\frac{4k_B T}{\omega} \Im\{T_F(\omega)\} \quad (24)$$

where $T_F(\omega) = \tilde{X}(\omega)/\tilde{F}_t(\omega)$ is the transfer function between the readout observable X and a force F applied with the same weight function P_s of the readout:³⁵

$$F(r, \theta, t) = F_t(t) P_s(r, \theta) \quad (25)$$

If we substitute this specific force field in the general solution Eq. (23), we find, at resonance ω_n :

$$T_F(\omega_n) = -i \frac{Q_n}{M \omega_n^2} \left(\int_S dS P_s(r, \theta) w_n(r, \theta) \right)^2 = -i \frac{Q_n}{\omega_n^2 m_n^{\text{eff}}} \quad (26)$$

where the effective mass has been defined in Eq. (12). From Eqs. (24) and (26), the thermal noise PSD on the output variable is:

$$S_{XX}(\omega_n) = 4k_B T \frac{Q_n}{m_n^{\text{eff}} \omega_n^3} \quad (27)$$

where m_n^{eff} for the circular membrane and for the gap modes of the rectangular soft-clamped membrane are evaluated respectively in Eqs. (13) and (17). The minimal detectable force is obtained by the comparison between the output X induced by the force \mathbf{G} and the noise power spectral density S_{XX} . The sensitivity of the device as a detector of this force is defined as the ratio:

$$S_{GG}(\omega_n) = \frac{S_{XX}(\omega)}{|T_G(\omega)|^2} \quad (28)$$

and should be as low as possible in the frequency range of interest. At resonance ω_n we can substitute equations (26) and (27) and obtain:

$$S_{GG}(\omega) = 4k_B T \frac{\omega_n}{Q_n} \frac{M}{\left(\int_V dV G_r(r, \theta, z) w_n(r, \theta) \right)^2} \quad (29)$$

that make clear the role of the modal shape on the sensitivity of the system. It is not surprising that low temperatures and high quality factors are of benefit to the measure, while the term depending on the modal shape is sometimes overlooked.

3. Point force

To study the case of a force applied in the center of the membrane, we assume for simplicity that it is directed along the membrane axis \mathbf{i}_z and applied onto the surface $z = 0$ with

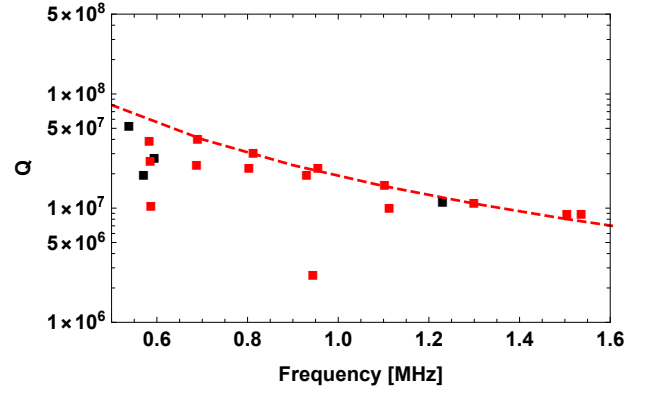


FIG. 14. Measured Q factors vs frequency for the bandgap mode A of a rectangular-shaped phononic membrane of thickness $h = 100$ nm and stress $\sigma = 0.918$ GPa. Red line is the theoretical curve derived using Eq. (15) and sets a theoretical limit for the 2-D phononic membrane. Data points are experimental results measured in our setup (black squares) or measured by Tsaturyan,²¹ (red squares). In this case, the experimental values are scaled according to Eq. (18) to allow a proper comparison when the membrane thickness or the internal stress is not the same as our devices.

the shape of the readout weight function $P_s(r, \theta)$. The correspondent force density is $\mathbf{U}(\mathbf{r}, t) = U_t(t) P_s(r, \theta) \delta(z) \mathbf{i}_z$, where $U_t(t)$ is the total applied force. The normalization of the density function is a consequence of the normalization of the weight function P_s . In this case equation 29 can be rewritten as:

$$\begin{aligned} S_{UU}(\omega_n) &= 4k_B T \frac{\omega_n}{Q_n} \frac{M}{\left(\int_S dS P_s(r, \theta) w_n(r, \theta) \right)^2} \\ &= 4k_B T \frac{\omega_n}{Q_n} m_n^{\text{eff}} \end{aligned} \quad (30)$$

The sensitivity of both devices is reported in Table II, where the results have also been extrapolated to cryogenic ($T = 4.2$) and ultracryogenic ($T = 14$ mK) temperatures. We have extrapolated from literature data the temperature dependence of the Q-factor for the soft-clamped membranes.²¹ On the contrary we have assumed a constant value of Q for round-shaped membranes.²⁰ Soft clamped membranes are in general more sensitive, thanks to their higher quality factor, but in both cases these figures outperform the pN sensitivities typical of atomic force microscopes, and push us to further improve the performance and stability of the production process.

4. Uniform force field

We consider now the sensitivity of the membranes to a uniform force density field oriented along the membrane axis, \mathbf{i}_z . In this case we have $G_r(r, \theta, z) = 1/V$ and Equation (29) becomes

$$S_{GG}(\omega) = 4k_B T \frac{\omega_n}{Q_n} \frac{M V^2}{\left(\int_V dV w_n(r, \theta) \right)^2} \quad (31)$$

that can be evaluated by FEM for the relevant modes. Here we focus on the vibrational modes in the bandgap of the soft-

TABLE II. Thermal noise limits to the sensitivity to a point force at room, cryogenic and ultra-cryogenic temperatures. RS-M: mode (0,1) of round shaped membrane resonator. PM- a : mode A of soft-clamped membrane with lattice parameter a . The laser waist w_0 of the read-out and the effective mass of the oscillator are reported in the table. The physical parameters of the devices are listed here. RS-M: $h = 100$ nm, $f = 284$ kHz, $Q = 8.7 \times 10^6$; PM-160: $h = 100$ nm, $f = 1.23$ MHz, $Q = 9.1 \times 10^6$; PM-346: $h = 100$ nm, $f = 630$ kHz, $Q = 19.3 \times 10^6$.

$S_{UU}^{1/2}$	$w_0[\mu\text{m}]$	$m_{eff}[\text{ng}]$	@ 300 [K]	@ 4.2 [K]	@ 14 [mK]
			$[a\text{N}/\sqrt{\text{Hz}}]$	$[a\text{N}/\sqrt{\text{Hz}}]$	$[a\text{N}/\sqrt{\text{Hz}}]$
RS-M	600	326	1014.13	119.98	6.92
RS-M	150	132	645.42	76.37	4.41
RS-M	50	125	627.85	74.29	4.28
PM-160	50	14.7	438.41	32.81	0.96
PM-346	50	38.0	329.51	24.61	0.72

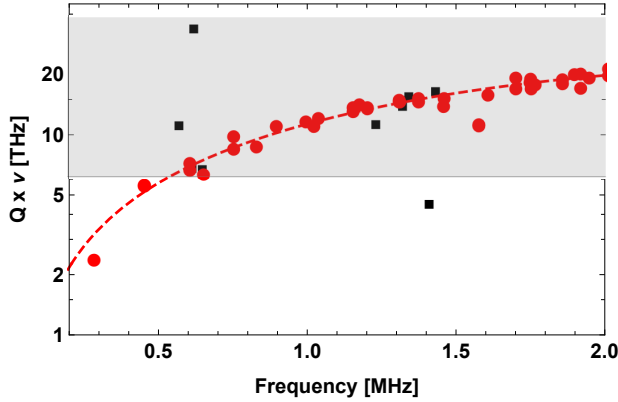


FIG. 15. The plot shows $Q \times v$ vs. frequency for the two membranes, at room temperature. Red circles refers to round-shaped membrane, black squares refers to modes (A, B, C, D) of soft-clamped membrane with lattice $a = 160 \mu\text{m}$ and $a = 360 \mu\text{m}$. The red-dashed line is the fitting model for the round shaped membranes. Data points within the gray shaded area fulfill the minimum requirement for quantum optomechanics at room temperature.

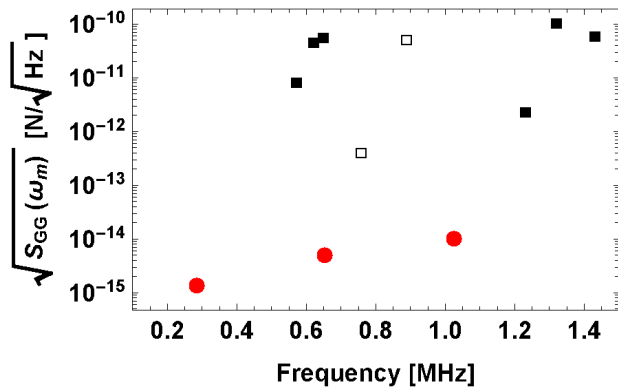


FIG. 16. Calculated force sensitivity $S_{GG}(\omega_m)$ at a temperature of 300 K for membrane based devices. Red circles correspond to lowest frequency axisymmetric modes of the round-shaped membrane while black squares correspond to bandgap modes A, B, C, D, E of the soft-clamped membrane. The empty black square refers to soft-clamped membrane with $a = 346 \mu\text{m}$ and thickness 35 nm described by Tsaturyan.²¹

clamped membrane and on the axisymmetric modes $(0, n)$ of the round-shaped membrane. Results are summarized in Figure (16), where we show the predictions for the membranes we have produced the laboratory and the ultra-high Q soft-clamped membrane described by Tsaturyan,²¹ featuring Q factors well over 10^7 . In general round-shaped membranes can detect an external uniform force with much higher sensitivity with respect to bandgap modes of the soft-clamped membrane. This is due to the peculiarity of soft-clamped membranes, where the matching of the defect modes and the phonon modes produce a modal shape that is confined in the defect area, as it is shown in Figure (5) for bandgap mode A. On the contrary, the axisymmetric modal shapes $(0, n)$ of round-shaped membranes are distributed over the whole membrane and allow a better matching of the modal shape with the uniform force field, even though their sensitivity decreases with the number of circumferential nodes. An estimation of the S/N in the case of specific force signals goes beyond the scope of the article.

VII. CONCLUSIONS

Freestanding nano-membranes initially became widespread as windows for chemical analysis by x-ray, e-beam and TEM, but recent studies have shown how useful they can be as highly coherent mechanical resonator in the field of quantum technologies and fundamental physics. In these optomechanical systems the membrane is embedded in a Fabry-Perot optical cavity, where the radiation pressure couples the membrane's mechanical displacement with the intracavity field. The high value of the mechanical quality factor, at cryogenic and room temperatures, guarantees basic requirements for many challenging experiments, such as ground state sideband cooling, quantum non demolition measurements and quantum squeezing of resonator states. Recent efforts are directed toward the functionalization of SiN membranes, to allow the coupling with external signals. We mention for instance the deposition of a metal layer for the realization of device capable of converting RF/microwaves to optical signals, possibly at the quantum limit.⁶

In this work we investigated the mechanical dissipation of

two state-of-the-art membrane-based devices used in quantum optomechanical experiments, both produced in our microfabrication facility. They are based on tensioned SiN membranes, with equal thickness and stress, and reach high Q-factors thanks to the dissipation dilution effect.¹⁵ Concepts based on stress/strain engineering and soft-clamping were used in the design to preserve this feature from the influence of the environment. A general design framework is outlined and discussed, showing advantages and drawbacks. We described the fabrication processes based on bulk/surface silicon micromachining and discussed our experimental results in the context of literature data.

Resonators with soft-clamping ensure the achievements of very high Q factor for a number of modes inside the bandgap, on the other hand we have observed that they are more fragile, as imperfections in holes edge can trigger the membrane failure during the release phase, handling or dicing. Currently, in the outcomes of our production process, the soft-clamped membranes are more sensitive to fabrication issues and we are reviewing the process to increase reproducibility and yield.

Circular-shaped membrane with loss shield constitutes a reliable platform for optomechanical experiments, with modal Q-factor almost constant over a large frequency band, but did not demonstrated quality factor higher than 10^7 . In this case we are studying how to apply a stress engineering approach to increase the quality factor for a membrane while maintaining a membrane thickness of 100 nm in the central region, as it is needed to facilitate the coupling with the laser beam.

We have completed our comparison with the evaluation of the interaction with an external force. As usual, we define the force sensitivity as the ratio between the thermal noise PSD and the square of the response function to the force. In the calculation we neglect back-action noise from the readout. The analysis show that the sensitivity is strongly dependent on the design of a device, with soft clamped membranes better suited for the detection of point forces while round shaped membranes have the best performance in the detection of uniform force fields. This issue is relevant in proposals aiming to use low-loss resonators in the detection dark matter signatures,³⁶ with an approach similar to that developed for a massive antenna.³⁷ We also note that in round-shaped membranes the Q-factor is obtained for a large number of modes, providing an ideal platform for multimode quantum optomechanics or multimode sensing.⁶

ACKNOWLEDGMENTS

Research was performed within the Project QuaSeRT funded by the QuantERA ERA-NET Cofund in Quantum Technologies implemented within the European Union's Horizon 2020 Programme. The research has been partially supported by INFN (HUMOR project).

¹D. Mason, J. Chen, M. Rossi, Y. Tsaturyan, A. Schliesser, Nat. Phys. **15**, 745 (2019).

²A. H. Ghadimi, S. A. Fedorov, N. J. Engelsens, M. J. Beryehi, R. Schilling, D. J. Wilson, T. J. Kippenberg, Science **360**, 764 (2018).

- ³A. Pontin, M. Bonaldi, A. Borrielli, L. Marconi, F. Marino, G. Pandraud, G. A. Prodi, P. M. Sarro, E. Serra, F. Marin, Phys. Rev. A **97**, 033833 (2018).
- ⁴M. Bawaj, C. Biancofiore, M. Bonaldi, F. Bonfigli, A. Borrielli, G. Di Giuseppe, L. Marconi, F. Marino, R. Natali, A. Pontin, G.A. Prodi, E. Serra, D. Vitali, F. Marin, Nat. Commun. **6**, 7503 (2015).
- ⁵A. Pontin, M. Bonaldi, A. Borrielli, F.S. Cataliotti, F. Marino, G. A. Prodi, E. Serra, F. Marin, Phys. Rev. A. **89**, (2014) 023848
- ⁶I. Moaddel Haghighi, N. Malossi, R. Natali, G. Di Giuseppe, D. Vitali, Phys. Rev. Applied **9**, 034031 (2018).
- ⁷R. W. Andrews, R. W. Peterson, T. P. Purdy, K. Cicak, R. W. Simmonds, C. A. Regal, K. W. Lehnert, Nat. Phys., **10**, (2014) 321
- ⁸M. Aspelmeyer, T. J. Kippenberg, F. Marquardt, Rev. Mod. Phys. **86**, 1391 (2014).
- ⁹Felix Tebbenjohanns, Martin Frimmer, Vijay Jain, Dominik Windey, and Lukas Novotny, Phys. Rev. Lett. **123**, 013603 (2020).
- ¹⁰U. Delić, M. Reisenbauer, K. Dare, D. Grass, V. Vuletić, N. Kiesel, M. Aspelmeyer, Science, **367**, 892 (2020).
- ¹¹L. Magrini, P. Rosenzweig, C. Bach, A. Deutschmann-Olek, S. G. Hofer, S. Hong, N. Kiesel, A. Kugi, M. Aspelmeyer, arXiv:2012.15188.
- ¹²A. Ranfagni, P. Vezio, M. Calamai, A. Chowdhury, F. Marino, F. Marin, arXiv:2012.15265.
- ¹³A. Pontin, M. Bonaldi, A. Borrielli, F.S. Cataliotti, F. Marino, G.A. Prodi, E. Serra, F. Marin, Phys. Rev. Lett. **112**, 023601 (2014).
- ¹⁴A. Chowdhury, P. Vezio, M. Bonaldi, A. Borrielli, F. Marino, B. Morana, G. A. Prodi, P.M. Sarro, E. Serra, F. Marin, Phys. Rev. Lett. **124**, 023601 (2020).
- ¹⁵P.R. Saulson, Phys. Rev. D **42**, 2437 (1990).
- ¹⁶Q. P. Unterreithmeier, T. Faust, J.P. Kotthaus, Phys. Rev. Lett. **105**, 027205 (2010).
- ¹⁷S. Schmid, K. D. Jensen, K. H. Nielsen, A. Boisen, Phys. Rev. B **84**, 165307 (2011).
- ¹⁸M. Bückle, V. C. Hauber, G. D. Cole, C. Gartner, U. Zeimer, J. Grenzer, E. M. Weig, Appl. Phys. Lett. **113**, 201903 (2018).
- ¹⁹S. Ghaffari, S. A. Chandorkar, S. Wang, E. J. Ng, C. H. Ahn, V. Hong, Y. Yang, T. W. Kenny, Sci. Rep. **3**, 3244 (2013).
- ²⁰A. Borrielli, L. Marconi, F. Marin, F. Marino, B. Morana, G. Pandraud, A. Pontin, G.A. Prodi, P. M. Sarro, E. Serra, M. Bonaldi, Phys. Rev. B **94**, 121403 (2016).
- ²¹Y. Tsaturyan, A. Barg, E. S. Polzik, A. Schliesser, Nat. Nanotechnol. **12**, 776 (2017).
- ²²D. R. Southworth, R. A. Barton, S.S. Verbridge, B. Ilic, A. D. Fefferman, H. G. Craighead, J. M. Parpia, Phys. Rev. Lett. **102**, 225503 (2009).
- ²³P.L. Yu, T. P. Purdy, C. A. Regal, Phys. Rev. B **108**, 083603 (2012).
- ²⁴L. Meirovitch, *Methods of analytical dynamics*, McGraw-Hill, New York, (1970).
- ²⁵S. A. Fedorov, N. J. Engelsens, A. H. Ghadimi, M. J. Beryehi, R. Schilling, D. J. Wilson, T. J. Kippenberg, Phys. Rev. B **99**, 054107 (2019).
- ²⁶M. J. Beryehi, A. Beccari, S. A. Fedorov, A. H. Ghadimi, R. Schilling, Dalziel J. Wilson, Nils J. Engelsens, Tobias J. Kippenberg, Nano Lett. **19**, 2329 (2019).
- ²⁷L. G. Villanueva, S. Schmid, Phys. Rev. Lett. **113**, 227201 (2014).
- ²⁸E. Serra, B. Morana, A. Borrielli, F. Marin, G. Pandraud, A. Pontin, G. A. Prodi, P. M. Sarro, M. Bonaldi, IEEE J. Microelectromech. Syst. **27**, 1193 (2018).
- ²⁹G. Gopalakrishnan, D. A. Czaplewski, K. M. McElhinny, M. V. Holt, J. C. Silva-Martínez, P. G. Evans, Appl. Phys. Lett. **102**, 033113 (2013).
- ³⁰E. Serra, M. Bawaj, A. Borrielli, G. Di Giuseppe, S. Forte, N. Kralj, N. Malossi, L. Marconi, F. Marin, F. Marino, B. Morana, R. Natali, G. Pandraud, A. Pontin, G. A. Prodi, M. Rossi, P. M. Sarro, D. Vitali, M. Bonaldi, AIP Advances **6**(6), 065004 (2016).
- ³¹A. Chowdhury, P. Vezio, M. Bonaldi, A. Borrielli, F. Marino, B. Morana, G. Pandraud, A. Pontin, G. A. Prodi, P. M. Sarro, E. Serra, F. Marin, Quantum Sci. Technol., **4**, 024007 (2019).
- ³²P. Vezio, A. Chowdhury, M. Bonaldi, A. Borrielli, F. Marino, B. Morana, G. A. Prodi, P. M. Sarro, E. Serra, F. Marin, Phys. Rev. A **102**, 053505 (2020).
- ³³M. Bonaldi, A. Borrielli, A. Chowdhury, G. Di Giuseppe, W. Li, N. Malossi, F. Marino, B. Morana, R. Natali, P. Piergentili, G. A. Prodi, P. M. Sarro, E. Serra, P. Vezio, D. Vitali, F. Marin, The European Physical Journal D, **74**, 178 (2020).
- ³⁴M. Bonaldi, M. Cerdonio, L. Conti, P. Falferi, P. Leaci, S. Odorizzi, G.

- A. Prodi, M. Saraceni, E. Serra, and J. P. Zendri, *Phys. Rev. D* **7**, 022003 (2006).
- ³⁵Yu. Levin, *Phys. Rev. D* **57**, 659 (1998).
- ³⁶D Carney, G. Krnjaic, D. C. Moore and C. A. Regal *Quantum Sci. Technol.* **6**, 024002 (2021).
- ³⁷A. Branca, M. Bonaldi, M. Cerdonio, L. Conti, P. Falferi, F. Marin, R. Mezzena, A. Ortolan, G. A. Prodi, L. Taffarello, et al., *Phys. Rev. Lett.* **118**, 021302 (2017).